HHS Public Access

Author manuscript

Anal Chem. Author manuscript; available in PMC 2019 August 07.

Nanoscale Intelligent Imaging Based on Real-Time Analysis of Approach Curve by Scanning Electrochemical Microscopy

Ryan J. Balla[†], **Dylan T. Jantz**[‡], **Niraja Kurapati**[†], **Ran Chen**[†,§], **Kevin C. Leonard**[‡,*], **Shigeru Amemiya**[†,*]

[†]Department of Chemistry, University of Pittsburgh, 219 Parkman Avenue, Pittsburgh, Pennsylvania, 15260, United States

[‡]Center for Environmentally Beneficial Catalysis, Department of Chemical and Petroleum Engineering, University of Kansas, 1501 Wakarusa Drive, Lawrence, Kansas 66047, United States

Abstract

Scanning electrochemical microscopy (SECM) enables high-resolution imaging by examining the amperometric response of an ultramicroelectrode tip near a substrate. Spatial resolution, however, is compromised for non-flat substrates, where distances from a tip far exceed the tip size to avoid artifacts caused by the tip–substrate contact. Herein, we propose a new imaging mode of SECM based on real-time analysis of approach curve to actively control nanoscale tip–substrate distances without contact. The power of this software-based method is demonstrated by imaging an insulating substrate with step edges using standard instrumentation without combination of another method for distance measurement, e.g., atomic force microscopy. An ~500 nm-diameter Pt tip approaches down to ~50 nm from upper and lower terraces of a 500 nm-height step edge, which are located by real-time theoretical fitting of experimental approach curve to ensure the lack of electrochemical reactivity. The tip approach to step edge can be terminated at <20 nm prior to the tip–substrate contact as soon as the theory deviates from the tip current, which is analyzed numerically afterward to locate the inert edge. The advantageous local adjustment of tip height and tip current at the final point of tip approach distinguishes the proposed imaging mode from other modes based on standard instrumentation. In addition, the glass sheath of Pt tip is thinned to ~150 nm to rarely contact the step edge, which is unavoidable and instantaneously detected as an abrupt change in the slope of approach curve to prevent the damage of fragile nanotip.

Graphical Abstract

[*]**Corresponding Author**: K. C. Leonard. kcleonard@ku.edu. Fax: 785-864-4967. S. Amemiya. amemiya@pitt.edu. Fax: 412-624-8611.

[§]**Present Addresses**: Department of Chemistry, University of Illinois at Urbana–Champaign, 600 South Mathews Avenue, Urbana, Illinois 61801, United States.

R.J.B. and D.T.J. equally contributed to this work.

Supporting Information

The Supporting Information is available free of charge on the ACS Publications website.

SEM images of tip, finite element simulation of characteristic approach curves, constant-height images, approach curves with multistep tip–substrate contact, and analytical expressions of approach curves at reactive substrates (PDF)

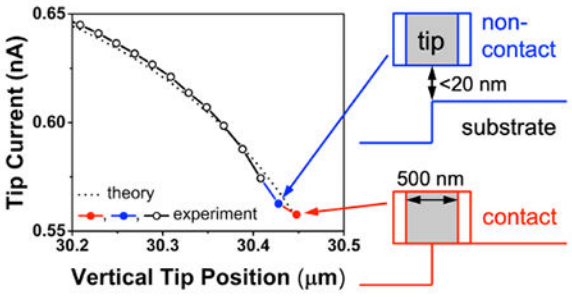

Accurate control of short distance between a tip and a substrate is crucial for high-resolution and non-contact imaging by scanning electrochemical microscopy[1–3] (SECM). The tip–substrate distance, *d*, limits the spatial resolution of SECM as represented by[4]

$$h^{\infty} = 1.5d + a \quad (1)$$

where h^{∞} is the radius of local substrate surface seen in the feedback mode and *a* is the radius of disk-shaped tip. It, however, is challenging to maintain short distances of $<a$ over non-flat substrates without the tip–substrate contact by using standard instrumentation[5] equipped with a tip positioner and a potentiostat.[6] This setup dominantly employs the constant-height imaging mode,[5] where a tip is scanned laterally at a fixed height to lose a feedback effect from a recession of substrate or crash the tip into a protrusion.[7] The standard setup is also operated in the constant-current imaging mode, which is straightforward only when the substrate is relatively flat and uniformly reactive.[8] Alternatively, SECM is combined with other techniques, e.g., atomic force microscopy, to determine the tip–substrate distance by the second method.[9] Combined SECM techniques, however, are not widely adopted,[10] because sophisticated hardware and complicated multifunctional probes are required.

The tip–substrate distance can be determined accurately from the strong distance-dependence of tip current[11] as represented by SECM approach curves.[4] Approach curves were measured at different lateral tip positions and analyzed only afterward to deconvolute the topography and reactivity of substrate.[10,12,13] The depth scan mode,[12,14] however, obtains approach curves by repeatedly imaging a substrate at different tip heights, thereby resulting in the same limitations as the constant-height mode. The intermittent contact mode[10] requires the simultaneous measurement of shear force between a tip and a substrate to terminate tip approach upon contact, which can damage the substrate[15] to artificially alter its topography and reactivity. The hopping mode was implemented into standard instrumentation with nanometer-sized tips to image biological cells[16] and glass-supported platinum microbands.[13] Non-contact imaging of these non-flat substrates terminated the tip approach when the tip current, i_T, decreased to only ~95% of that in the bulk solution, $i_{T,\infty}$. The resultant long tip–substrate distance of ~5a at insulating substrates[17] largely compromises the spatial resolution.

Herein, we propose a new imaging mode of SECM based on real-time analysis of approach curve to actively control nanoscale tip–substrate distances without contact. In contrast to combined SECM techniques,[9] this imaging mode employs standard instrumentation equipped with a disk-shaped nanotip[18,19] and controlled by the advanced version of Labview-based software,[20,21] which measures and analyzes the tip current after each step of tip approach to substrate. The power of this software-based method is demonstrated by high-resolution and non-contact imaging of an insulating substrate with step edges (Figure 1). Specifically' short distances of ≤0.3*a* are achieved without contact when a glass-sealed Pt nanotip approaches not only flat terraces (Figures 1A and B) to yield a good fit between experimental and theoretical approach curves, but also step edges (Figure 1C), which are located by a deviation of the tip current from the theory as explained by the post-imaging analysis of the approach curve. The thin glass sheath with a small outer radius, r_g, rarely contacts the step edge (Figure 1D), which is unavoidable and instantaneously detected as an abrupt change in the slope of approach curve to prevent the damage of fragile nanotip. The general applicability of this imaging mode to substartes with various topography and reactivity is also discussed.

EXPERIMENTAL SECTION

Chemicals and Materials.

$Ru(NH_3)6Cl_3$ was obtained from Strem Chemicals (Newburyport, MA). KCl (≥99%) was purchased from Sigma Aldrich (Milwaukee, WI). Insulating SiO_2/Si substrates with step edges (HS-500MG-UM) were obtained from Ted Pella (Redding, CA) and characterized by SEM (Figure 2). A Milli-Q Advantage A10 system combined with Elix 3 Advantage (EMD Millipore, Billerica, MA) purified tap water to obtain the resistivity of 18.2 MΩ·cm and the total organic carbon of 2–3 ppb.[22]

SECM Imaging.

A home-built SECM instrument[21] was equipped with a potentiostat (CHI 802D, CH Instruments, Austin TX) and controlled by using the Labview program based on a custom fuzzy logic algorithm[20] (National Instruments, Austin, TX). An SECM stage was accommodated in a faraday cage equipped with metallic heat sinks and surrounded by polystyrene foams[21] to maintain stable temperature and, subsequently, minimize thermal drift.[23] Pt tips with inner and outer radii of ~0.25 and ~0.4 μm, respectively, were fabricated by laser-assisted pulling, heat annealing, and focused-ion-beam (FIB) milling[24,25] and characterized by scanning electron microscopy (SEM; Figure S-1). The tips were protected from electrostatic discharge[26] under sufficiently high humidity (>30%)[27] as well as from electrochemical damage by using the cell-on-between-run function of the modified potentiostat.[28] Pt wires served as counter and quasi-reference electrodes. The tip potential was set to obtain the steady-state current based on the diffusion-limited reduction of 10 mM $Ru(NH_3)_6^{3+}$ in 1 M KCl.

RESULTS AND DISCUSSION

Simulation of Approach Curves at Step Edge.

The development of imaging algorithm (see below) was facilitated by finite element simulation of approach curves at step edges of insulating substrate. Interestingly, simulated approach curves are unique and different from those simulated and observed experimentally at flat substrates that were vertical or slightly tilted against a tip.[29–31] Finite element simulation was performed by solving a 3D diffusion problem with a disk-shaped SECM tip with $RG = 1.5$ (= r_g/a) approaching a step edge with a height of tip diameter, $2a$ (Figure S-2).

Figure 3 shows characteristic approach curves simulated at the step edge of insulating substrate. When a tip approaches to the upper terrace far from the step edge (Figure 1A), the theoretical current based on the negative feedback effect, i_T^{NF}, is given by[17]

$$\frac{i_T^{NF}}{i_{T,\infty}} = \frac{\frac{2.08}{RG^{0.358}}\left(L - \frac{0.145}{RG}\right) + 1.585}{\frac{2.08}{RG^{0.358}}(L + 0.0023RG) + 1.57 + \frac{\ln RG}{L} + \frac{2}{\pi RG}\ln\left(1 + \frac{\pi RG}{2L}\right)} \quad (2)$$

where $L = d/a$. A higher tip current is expected when a larger part of Pt tip is positioned over the lower terrace (magenta, orange, and blue lines in Figure 3) until the edge of tip barely contacts the step edge (dashed line). Higher tip currents are attributed to less hindered diffusion of redox species from the solution above the lower terrace to the tip (Figures 1C and D). By contrast, the tip current is lower than eq 2 when the edge of tip just passes the step edge to approach the lower terrace (red line in Figure 3). The tip current is lowered by a negative feedback effect from the wall of step edge (Figure 1B), which hinders the diffusion of redox species to the tip. The additional negative feedback effect becomes smaller over the lower terrace further from the step edge to eventually follow eq 2.

Imaging Algorithm.

We implemented a new algorithm into Labview software[20,21] (Figure 4) to enable SECM imaging based on real-time analysis of approach curve. This algorithm aims at vertically bringing the tip to the proximity of a substrate to achieve high spatial resolution without tip–substrate contact. The current version of the software targets insulating substartes by employing eq 2 but will be applicable to reactive substartes by employing the corresponding equations as discussed later. Specifically, the stepwise tip approach to substrate is followed by the measurement of steady-state tip current. When the tip–substrate distance is short enough to yield $i_T < 0.90 i_{T,\infty}$, the occurrence of tip–substrate contact is judged from a change in the slope of approach curve as detailed below. Without contact, the measured current is compared with a theoretical value predicted by eq 2, which is fitted to all previous data points by adjusting $i_{T,\infty}$ and z tip position at $L = 0$ using the Virtual Instrument of Labview for nonlinear curve fit. A difference between experimental and theoretical currents, Δi_T, is defined as

$$\Delta i_T = i_T - i_T^{NF} \quad (3)$$

When Δi_T exceeds a preset value, the tip approach is terminated to achieve the shortest non-contact distance, e.g., at step edges (Figure 1C). Otherwise, the tip current is compared with a preset threshold value of $0.4 i_{T,\infty}$, which corresponds to $d = 0.3a$ with $RG = 1.5$ in eq 2. The threshold current is reached when the tip approaches an upper terrace far from the step edge (Figure 1A) or a lower terrace (Figure 1B). In these cases, the entire approach curve is fitted with eq 2 to determine the z tip position at $L = 0$ as the vertical position of substrate for topography imaging. If the tip current is still higher than the threshold value, the fuzzy logic algorithm of Labview[20] is used to move the tip closer to the substrate with a smaller step than the last step. This fuzzy logic algorithm employs a non-Boolean control system that uses input variables (e.g., tip size, enhancement factor, and distance from target set-point) to continuously change the step size of the approach smoothly, and automatically stop the tip at a given setpoint. A smaller step at a shorter tip–substrate distance not only records the steeper part of approach curve accurately, but also minimizes the damage of tip[32] and substrate[15] upon their contact.

Our algorithm evaluates a change in the slope of approach curve, Δslope, to detect the tip–substrate contact. Negative approach curves at an insulating substrate (Figure 3) become monotonically steeper at a shorter tip–substrate distance. By contrast, the slope of approach curve becomes smaller when the tip–substrate contact occurs to limit a change in the tip current, thereby yielding

$$\Delta\text{slope} = |\Delta i_n|/\Delta z_n - |\Delta i_{n-1}|/\Delta z_{n-1} < 0 \quad (4)$$

where Δi_n and Δz_n are changes in tip current and vertical tip position, respectively, after the nth step of tip approach. The tip–substrate contact results in Δslope more negative than an empirically preset value, which is not zero, because of the noise of tip current.

Line Scan over Step Edges.

We tested the algorithm based on real-time analysis of approach curve by performing line scan over step edges. In this test, the entire profile of approach curves at step edges was obtained by bringing a tip to a substrate until the tip–substrate contact occurred at Δslope < −0.1 pA/nm (see eq 4), thereby yielding detailed information about differences between experimental and theoretical currents, Δi_T (eq 3), as assessed below. Specifically, a 400 nm-diameter Pt tip with $RG = 1.6$ was used to obtain approach curves with a lateral interval of 100 nm over three edges of 500 nm-deep square-shaped recessions with a length of 6 μm and an interval of 4 μm as determined by SEM (Figure 2). The tip current was based on the diffusion-limited reduction of 10 mM $Ru(NH_3)_6^{3+}$, where $i_{T,\infty}$. is given by

$$i_{T,\infty} = 4xnFDc_0a \quad (5)$$

where x is a function of RG[33], n (= 1) is the number of transferred electrons, and D (= 7.8 × 10^{-6} cm^2/s) and C_0 are its diffusion coefficient and concentration of $Ru(NH_3)_6^{3+}$, respectively. $Ru(NH_3)_6^{3+}$ yields a stable $i_{T,\infty}$ value to enable the quantitative analysis of approach curves, where non-ideal tip behaviors must be prevented, e.g., as demonstarted by programming the tip potential for O_2.[34]

Figure 5 shows the time profile of the tip current during the measurement of 151 approach curves at different lateral tip positions over three step edges. The tip initially approached the lower terrace, where the tip current went below a threshold value of 0.40iT,,,, (red fine). The tip was closest to the step edge (Figure 1B) when the last approach curve in red was obtained. The next approach curve (blue fine) was obtained when the glass sheath of a tip approached the edge (Figure 1D), where the tip current decreased only to ~80% of $i_{T,\infty}$ upon the tip–substrate contact as predicted theoretically (e.g., blue line in Figure 3). The next four approach curves also failed to reach a threshold current of $0.40i_{T,\infty}$, where a part of the tip approached to the edge (Figure 1C) to yield higher tip currents even at L = 0 as predicted theoretically (e.g., orange fine in Figure 3). Eventually, the threshold tip current was obtained to terminate the tip approach at the next lateral position, where the entire tip approached the upper terrace of the substrate (Figure 1A). Two other edges also gave similar characteristic approach curves.

The line-scan experiment quantitatively revealed the topography of substrate including the location of step edges. Specifically, each approach curve was fitted with eq 2 to yield a z tip position at L = 0 (red and blue circles in Figure 6A). This tip position corresponded to the actual position of the substrate surface when the tip current went below the threshold (Figure 6B). The resultant profile represents the height of step edges (500 nm) and traces the tilt of the substrate. The gradual change of substrate position is not due to the thermal drift of initial vertical tip position,[21,23] which was minimized by an isothermal chamber.[21,23] Importantly, the vertical tip position at the last point of approach curve (black circles in Figure 6A) was only ~50 nm away from terraces of the substrate. By contrast, the z tip position at L = 0 is not equivalent to the position of the substrate near step edges, where experimental approach curves did not fit well with eq 2 (see below). The tip current at the last point of each approach curve was much higher than the threshold value of $0.40i_{T,\infty}$ when the tip approached step edges (Figure 6B). Nevertheless, we were able to accurately locate step edges (dotted lines in Figure 6), which were separated by ~r_g (= ~400 nm) from the lateral tip position when the tip approached the lower terrace to barely pass the step edge (Figure 1B). The separation between step edges corresponds to 6.0 and 3.9 μm in the line scan (Figure 6) as expected from length and separation of recession (6.0 and 4.0 μm, respectively, in Figure 2).

Characteristic Approach Curves.

Here, we use characteristic approach curves from the line scan experiment (Figure 5) to assess differences between experimental and theoretical tip currents, Δi_T (eq 3), at various lateral tip positions. Specifically, Figure 7 shows characteristic experimental approach curves (circles) and best-fitted theoretical curves (lines) in addition to Δi_T values determined at each vertical tip position when $i_T < 0.90i_{T,\infty}$. The line scan experiment employed a large

threshold value for Δi_T of 10 nA, which was never exceeded. Accordingly, approach curves were measured until the tip–substrate contact occurred or when the tip current went below a threshold value.

The tip current followed eq 2 to go below a preset threshold of $0.40 i_{T,\infty}$ at lower and upper terraces far from the edge (red and blue lines, respectively, in Figure 7A). The resultant Δi_T values (crosses in Figure 7A) were very small and ranged between ±3 pA (i.e., ±0.4% of $i_{T,\infty}$), which is attributed to the noise of tip current. The theoretical curves were fitted best by adjusting z positions at $L = 0$ to 30.876 and 30.399 μm for lower and upper terraces, respectively. The difference of z positions (477 nm) is close to but is slightly smaller than the height of step edge (500 nm), which is attributed to the tilt of substrate (Figure 6A). The lateral positions of these two approach curves are separated by 6 μm to yield a tilt angle of 2.2° from the height difference of 23 nm.

Figure 7B shows a characteristic approach curve at the lower terrace adjacent to the step edge (Figure 1B), which importantly features large positive Δi_T values. As expected from simulation (red line in Figure 3), the experimental approach curve showed a “dip” when the tip was positioned below the upper terrace, where the diffusional access of $Ru(NH_3)_6^{3+}$ to the Pt tip was partially hindered by the wall of step edge (Figure 1B). Eventually, the tip current dropped to $0.40 i_{T,\infty}$ without the contact of the tip with the flat lower terrace. The approach curve, however, did not fit with eq 2 at relatively long distances, even when a lower $i_{T,\infty}$ value was used in the theoretical curve (solid line in Figure 7B), thereby requiring a long time for fitting to broaden the corresponding part of current-time profile in Figure 5. Overall, the experimental tip current at the last data point was always higher than the theoretical value (see the inset) to yield a large positive Δi_T value. Nevertheless, the adjusted z position at $L = 0$ was consistent with the position of the lower terrace (Figure 6A).

Negative Δi_T values were obtained before the tip–substrate contact (Figure 7C) when the tip approached the step edge of the substrate as depicted in Figure 1C. The tip current at this location is expected to be higher than eq 2 (Figure 3), because the Pt tip is only partially blocked by the upper terrace and is partially exposed to the lower terrace. Accordingly, the theoretical curve was shifted laterally to minimize the sum of least squares, thereby yielding negative Δi_T values except for the contact point, where $\Delta i_T > 0$ (see the inset). This result indicates that the tip–substrate contact was avoidable selectively at step edges by setting a relatively large and negative threshold for Δi_T, which is small at upper terraces (Figure 7A) and positive at lower terraces (Figure 7B).

We assessed 151 approach curves in the line scan to find that the tip–substrate contact was unavoidable for one approach curve (Figure 7D), where the glass sheath of tip barely contacted the edge of the substrate (Figure 1D). This approach curve fitted very well with eq 2 until the tip contacted the substrate to deviate the tip current positively from eq 2 (see the inset). Before the contact, Δi_T values were as small as observed at lower and upper terraces far from step edges (Figure 7A). Therefore, any threshold value for Δi_T can not avoid the contact between very edges of tip and substrate. Remarkably, closest tip–substrate distances just before contact with step edges were only ~20 nm (see insets of Figures 7C and 7D), which corresponds to a small step size as adjusted by the fuzzy logic algorithm near the

substrate[20] (Figure 7). This result indicates that a small negative Δslope value (see eq 4) can sensitively and immediately detect the tip–substrate contact to avoid the damage of fragile nanotips (see below).

It should be noted that the SECM line scan experiment not only obtained emipirical threshold Δi_T values for non-contact imaging (see below) but also determined the topography and inert reactivity of step edges, where experimental approach curves that did not fit eq 2 (Figures 7B, 7C, and 7D) agreed remarkably well with approach curves simulated by the finite element method (Figures S-4A, S-4B, and S-4C, respectively). The post-imaging analysis of approach curves proved that the negative feedback effect from the wall of step edge resulted in the dip of the approach curve (Figure S-4A). The numerical analysis also ensured that high tip currents at the contact between the tip and the edges (Figures S-4B and S-4C) are due to a topographic effect not the local reactivity of substrate.

Non-Contact Intelligent Imaging.

We employed real-time analysis of the approach curve to enable high-resolution and non-contact imaging of 6 μm-long square-shaped protrusion and recession surrounded by 500 nm-high step edges. A lateral step size of 1 μm was large enough to minimize a chance of positioning the glass sheath of tip over the step edge of the substrate, where the tip–substrate contact is unavoidable. A threshold value of $0.40 i_{T,\infty}$ was set to terminate the tip approach at the lower terrace and the upper terrace far from step edges. The tip approach at step edges was terminated when Δi_T became more negative than a small negative threshold of −11 pA (i.e., −1.5% of $i_{T,\infty}$) as determined empirically from line scans. This negative threshold was not exceeded when the tip approached the lower terrace near the step edge, where Δi_T was larger but positive (see Figure 7B). Non-contact imaging was ensured, because Δslope did not exceed a threshold value of −0.1 pA/nm established above.

Non-contact images of 6 μm × 6 μm protrusion were obtained by using the position of substrate surface determined by fitting approach curves with eq 2 (Figure 8A) as well as the tip current at the last point of approach curves (Figure 8B). The former image represents the topography of protrusion to determine not only its length of 6 μm but also its height of ~0.5 μm. The latter represents a reactivity image, which ensures the inert reactivity of upper and lower terraces. In addition, tip currents at edges are higher to represent not the local reactivity of the substarte but the less hindered diffusion of $Ru(NH_3)_6^{3+}$ from the solution over the lower terrace to the Pt tip. Even higher tip currents were observed at corners of recession, where the tip is exposed more to the lower terrace (Figure S-3A). In the reactivity image, the tip current reached the threshold value at the right edge of protrusion, which is dislocated toward the right-hand side as indicated by dashed lines to lower the tip current. Interestingly, the lateral asymmetry of image based on the tip current is more enhanced than that of topography image to enable the more accurate location of step edges.

Importantly, the intelligent mode provides complimentary topography and reactivity images to unambiguously determine the height of step edges and the inertness of terraces, respectively, in contrast to a constant-height image based on the convolution of topography and reactivity (Figure S-5A). The constant-height mode yielded a lower tip current over the insulating protrusion, which is closer to the tip than the surrounding insulating region to

exert a larger negative feedback effect on the tip current. This interpretation, however, is based on our prior knowledge of substrate inreness and topography. Without this knowledge, the constant-height image can be interpreted in a variety of ways, for instance, as an image of a flat substrate with a more reactive surrounding. Similarly, the topography and reactivity of substrate will be convoluted in a constant-current image of the non-flat substrate with step edges, where the tip current drops only to $0.8i_{T,\infty}$. A constant tip current of $>0.8i_{T,\infty}$ must be set even over flat regions to prevent the unambiguous determination of their inertness and position.

Both topography and reactivity images of 6 μm × 6 μm recession were obtained without the tip–substrate contact (Figures 8C and 8D, respectively). The recessed region was located by bringing the tip to its central region with dimensions of 5 μm × 5 μm as clearly shown in both images. The tip approached step edges just outside of the central region to yield higher tip currents at 7 μm × 7 μm frame (Figure 8D), where the diffusion of $Ru(NH_3)_6^{3+}$ to the tip was less hindered. Interestingly, the tip current was higher at edges than corners, where the Pt tip was less exposed to the solution over the lower terrace (Figure S-3B). Moreover, the tip current reached the threshold value at top corners, but not bottom corners, which indicates that the recession was dislocated downward in the image as indicated by dashed lines. Again, step edges were located more accurately by the enhanced asymmetry of the image based on the tip current to demonstrate its utility. The topography image measures the depth of recession (−0.5 μm) and the tilt of the substrate along the vertical axis as emphasized at the upper terrace. Complimentarily, the reactivity image ensured the inertness of upper and lower terraces. By contrast, the corresponding constant-height image of a recession (Figure S-5B) can be misinterpreted without the prior knowledge of substrate topography or reactivity to assign the higher tip current over the recessed central region to higher reactivity.

It should be noted that unavoidable contact between the glass sheath of the tip and the step edge of substrate occurred occasionally but did not damage tips as shown by SEM after imaging (Figures 9A and 9B). The tips were not damaged, not only because small step sizes of 20 nm or less were used during the tip approach, but also because the tips were retracted as soon as the tip–substrate contact was indicated by an abrupt change in the slope of approach curve. Tips were seriously damaged when the tips were pushed further to a substrate after the initial tip–substrate contact during imaging of recession and protrusion (Figures 9C and 9D, respectively). In these cases, a high threshold value of −0.5 pA/nm was set for Δslope (see eq 4) to cause the multiple-step contact as demonstrated by the corresponding approach curves (Figure S-6). The time profile of tip current (Figure S-7) showed a sudden increase in $i_{T,\infty}$ when the glass sheath near the Pt tip was cracked (Figure 9C), but not when only the glass sheath was damaged (Figure 9D). The approach curves were analyzed to determine total step sizes of −100 nm after the tip–substrate contact (Figure S-6). These total step sizes are comparable to those of intermittent contact mode, where a tip was pushed toward a substrate by three steps of 50 nm after the initial tip–substrate contact to ensure that the damping of tip vibration well exceeds the noise level.[10]

Imaging Time.

Here, we assess the imaging time of the proposed method, which is intrinsically long but can be improved significantly. The measurement and analysis of the approach curve at every lateral tip position requires longer imaging time than constant-height and constant-current modes. In this work, the measurement of the approach curve took twice longer than its real-time analysis. In the algorithm shown in Figure 4, it took ~0.1 s to move and stabilize the tip position before the tip current was measured and averaged for ~0.1 s. Then, it took ~0.1 s to quantitatively analyze the approach curve. The majority of analysis time was spent for non-linear fitting, which was even longer when a good fit was not obtained for approach curves at lower terraces adjacent to the edge, i.e., curve 4 in Figure 5. Overall, it took ~40 min for the measurement of 151 approach curves in line scan (Figure 5) and ~32 min for 121 approach curves in imaging (Figure 8), which corresponds to ~16 s per approach curve with ~50 points. A travel distance of ~5 μm for each approach curve yields an apparent velocity of ~0.3 μm/s. This velocity is similar to a velocity of ~0.3 μm/s employed in the intermittent contact mode,[10] which is also intrinsically slow.

The speed of approach curve measurement can be made much faster by employing instrumentation developed for fast scanning ion-conductance microscopy.[35] For instance, an ionic current of ~2.7 nA was measured with a precision of ±0.5 pA (i.e., ±0.02% of the ionic current) when an ~100 nm-diameter water-filled nanopipet traveled 2 μm in 4–40 ms, i.e., 50–500 μm/s.[36] In comparison with our setup, not only was the similar current measured more precisely despite much faster sampling, but also the approach velocity was ~100–1000 times faster. Importantly, this high velocity is still slow enough to measure the current response of SECM nanotips under diffusion-limited steady-state conditions, which were also assumed for SECM theory (e.g., eq 2). These conditions are satisfied at up to the maximum velocity of tip approach to an insulating substrate, v_{max}, given by[37]

$$v_{max} = \frac{D}{a}\frac{RG}{115 + 22RG^{1.9}} \quad (6)$$

where an error of 2% is anticipated. Eq 6 with $D = 1 \times 10^{-5}$ cm^2/s gives a high v_{max} value of ~35 μm/s for Pt tips with $a = 0.25$ μm and $RG = 1.5$ as used in this study. An even higher v_{max} value of ~600 μm/s is obtained for nanopipet tips with $a = 15$ nm and $RG = 1.4$ as used in our previous studies.[38,39] With these high velocities, the imaging time is limited by real-time analysis of approach curves, which may be accelerated by using a fast computing method, e.g., quantum computing.[40]

It should be noted that the imaging mode proposed in this work is feasible by using micrometer-sized tips, but is less practical, because the slower tip approach to a substrate is required to avoid a convection effect on the tip current. Eq 6 yields a v_{max} value of ~0.4 μm/s for a tip with $a = 12.5$ μm and $RG = 10$. Moreover, a larger tip with lower distance sensitivity is used for imaging a larger topographic profile, which increases the travel distance of approach curve and, subsequently, imaging time. Previously, SECM topography imaging was enabled by moving a micrometer-sized tip ($a = 12.5$ μm) to insulating and

conductive substrates at 40 μm/s to obtain the transient convection-controlled tip current that was independent of substrate reactivity.[41]

General Applicability.

We envision that the proposed imaging method will be generally applicable to quantitatively determine the topography and reactivity of various substrates by analyzing experimental approach curves both in real time and after imaging complimentarily. For real-time analysis, eq 2 can be combined or replaced with analytical expressions for flat substartes with various reactivities to cover a wide spectrum of approach curves from purely negative ones to purely positive ones.[24,33,42] These analytical expressions are similar to each other (see Supporting Information) and will be adoptable into our future software straightforwardly. By contrast, the tip approach can be terminated without the tip–substrate contact when an experimental approach curve deviates from theoretical curves for any reason, e.g., the local non-flatness of the substrate. The resultant experimental approach curve can be analyzed numerically after imaging to determine the local topography and reactivity of the substarte, which are manifested as causes of the deviation. In this work, experimental approach curves near or at step edges were fitted well not by real-time analysis based on eq 2 (Figures 7B, 7C, and 7D) but by post-imaging analysis based on the finite element method (Figures S-4) to locate non-reactive step edges. This result suggests that the numerical analysis of approach curves will be useful for non-flat substartes with various reactivities.

CONCLUSIONS

In this work, a new imaging mode of SECM was proposed by implementing the real-time analysis of the approach curve for the first time, thereby enabling active control of nanometer tip–substrate distances without contact. In contrast to combined SECM techniques,[9] this imaging mode is based on standard instrumentation, which is controlled by the advanced version of Lab-view-based software[20,21] and equipped with a nanotip[18,19] to quickly yield steady-state diffusion-limited current without a convection effect.[37] This powerful operation mode yielded high-resolution and non-contact images of the insulating substrate with step edges. Advantageously, the step height and inert reactivity of substrate were unambiguously determined from topography and reactivity images (Figure 8), respectively, as obtained by locally adjusting tip height (Figure 6A) and threshold tip current (Figure 6B) to maintain short tip–substrate distances and, subsequently, high spatial resolution (eq 1). By contrast, other imaging modes based on standard instrumentation employ constant heights[5,12,14] or a constant threshold current,[8,13,16] where long distances from non-flat substrates are used for non-contact imaging to compromise the lateral spatial resolution and the accuracy of inert reactivity and step height of substrate.

SECM imaging based on real-time analysis of approach curve can be more versatile and robust to image the topography and reactivity of various substrates. Analytical theories are available for diskshaped tips at flat substrates with a wide range of electrochemical reversibility[24,33,42] as diverse guidelines to decide whether a tip can approach closer to a substrate without contact. The topography and reactivity of substrate can be determined in real time from good fits between experimental and theoretical curves or after imaging by the

numerical analysis of experimental approach curves, which are terminated as soon as the tip current deviates from theoretical curves. The numerical analysis requires the further exploration of approach curves at non-flat substrates, which will yield new fundamental insights into SECM. Ultimately, theoretical curves may be replaced with characteristic approach curves that are measured at different locations of a target substrate and numerically analyzed in advance. This empirical approach may be reinforced by machine learning,[43] where experimental approach curves from previous images are accumulated and used as guidelines to stop the tip approach immediately before the tip–substrate contact.

Supplementary Material

Refer to Web version on PubMed Central for supplementary material.

ACKNOWLEDGMENT

This work was supported by the National Institutes of Health (R01 GM112656). D.T.J. and K.C.L also acknowledge funding through the Army Research Office Young Investigator Grant No. 66446-CH-YIP (Award Number W911NF-17-1-0098).

REFERENCES

(1). Amemiya S; Bard AJ; Fan F-RF; Mirkin MV; Unwin PR Scanning electrochemical microscopy. Annu. Rev. Anal. Chem 2008, 1, 95–131.

(2). Bard AJ; Mirkin MV, Scanning electrochemical microscopy. 2nd ed.; Tayler and Francis: New York, 2012.

(3). Amemiya S, Scanning electrochemical microscopy of nanopores, nanocarbons, and nanoparticles In Nanoelectrochemistry, Mirkin MV; Amemiya S, Eds. Taylor and Francis: Boca Raton, FL, 2015; pp 621–653.

(4). Bard AJ; Mirkin MV; Unwin PR; Wipf DO Scanning electrochemical microscopy. 12. Theory and experiment of the feedback mode with finite heterogeneous electron-transfer kinetics and arbitrary substrate size. J. Phys. Chem 1992, 96, 1861–1868.

(5). Kwak J; Bard AJ Scanning electrochemical microscopy. Apparatus and two-dimensional scans of conductive and insulating substrates. Anal. Chem 1989, 61, 1794–1799.

(6). Fan F-RF; Bard AJ; He P, Instrumentation In Scanning electrochemical microscopy, 2nd ed.; Bard AJ; Mirkin MV, Eds. Tayler and Francis: New York, 2012; pp 15–23.

(7). Amemiya S; Guo J; Xiong H; Gross DA Biological applications of scanning electrochemical microscopy: Chemical imaging of single living cell and beyond. Anal. Bioanal. Chem 2006, 386, 458–471. [PubMed: 16855816]

(8). Wipf DO; Bard AJ; Tallman DE Scanning electrochemical microscopy. 21. Constant-current imaging with an autoswitching controller. Anal. Chem 1993, 65, 1373–1377.

(9). O'Connell MA; Wain AJ Combined electrochemical-topographical imaging: A critical review. Anal. Methods 2015, 7, 6983–6999.

(10). Lazenby RA; McKelvey K; Unwin PR Hopping intermittent contact-scanning electrochemical microscopy (HIC-SECM): Visualizing interfacial reactions and fluxes from surfaces to bulk solution. Anal. Chem 2013, 85, 2937–2944. [PubMed: 23373422]

(11). Wei C; Bard AJ Scanning electrochemical microscopy XXIX. In situ monitoring of thickness changes of thin films on electrodes. J. Electrochem. Soc 1995, 142, 2523–2527.

(12). Zhang MMN; Long Y-T; Ding Z Cisplatin effects on evolution of reactive oxygen species from single human bladder cancer cells investigated by scanning electrochemical microscopy. J. Inorg. Biochem 2012, 108, 115–122. [PubMed: 22169205]

(13). Jedraszko J; Michalak M; Jonsson-Niedziolka M; Nogala W Hopping mode SECM imaging of redox activity in ionic liquid with glass-coated inlaid platinum nanoelectrodes prepared using a heating coil puller. J. Electroanal. Chem 2018, 815, 231–237.

(14). Filice FP; Li MSM; Henderson JD; Ding ZF Threedimensional electrochemical functionality of an interdigitated array electrode by scanning electrochemical microscopy. J. Phys. Chem. C 2015, 119, 21473–21482.

(15). Lazenby R; McKelvey K; Peruffo M; Baghdadi M; Unwin P Nanoscale intermittent contact-scanning electrochemical microscopy. J. Solid State Electrochem 2013, 17, 2979–2987.

(16). Takahashi Y; Shevchuk AI; Novak P; Babakinejad B; Macpherson J; Unwin PR; Shiku H; Gorelik J; Klenerman D; Korchev YE; Matsue T Topographical and electrochemical nanoscale imaging of living cells using voltage-switching mode scanning electrochemical microscopy. Proc. Natl. Acad. Sci. U. S. A 2012, 109, 11540–11545. [PubMed: 22611191]

(17). Cornut R; Lefrou C A unified new analytical approximation for negative feedback currents with a microdisk SECM tip. J. Electroanal. Chem 2007, 608, 59–66.

(18). Amemiya S, Nanoscale scanning electrochemical microscopy In Electroanalytical chemistry, Bard AJ; Zoski CG, Eds. CRC Press: 2015; pp 1–72.

(19). Kai T; Zoski CG; Bard AJ Scanning electrochemical microscopy at the nanometer level. Chem. Commun 2018, 54, 1934–1947.

(20). Barforoush JM; McDonald TD; Desai TA; Widrig D; Bayer C; Brown MK; Cummings LC; Leonard KC Intelligent scanning electrochemical microscopy tip and substrate control utilizing fuzzy logic. Electrochim. Acta 2016, 190, 713–719.

(21). Pathirathna P; Balla RJ; Jantz DT; Kurapati N; Gramm ER; Leonard KC; Amemiya S Probing high permeability of nuclear pore complexes by scanning electrochemical microscopy: Ca^{2+} effects on transport barriers. Anal. Chem 2019, 91, 5446–5454. [PubMed: 30907572]

(22). Nioradze N; Chen R; Kurapati N; Khyataeva-Domanov A; Mabic S; Amemiya S Organic contamination of highly oriented pyrolytic graphite as studied by scanning electrochemical microscopy. Anal. Chem 2015, 87, 4836–4843. [PubMed: 25843146]

(23). Kim J; Shen M; Nioradze N; Amemiya S Stabilizing nanometer scale tip-to-substrate gaps in scanning electrochemical microscopy using an isothermal chamber for thermal drift suppression. Anal. Chem 2012, 84, 3489–3492. [PubMed: 22462610]

(24). Nioradze N; Kim J; Amemiya S Quasi-steady-state voltammetry of rapid electron transfer reactions at the macroscopic substrate of the scanning electrochemical microscope. Anal. Chem 2011, 83, 828–835. [PubMed: 21175129]

(25). Kim J; Izadyar A; Nioradze N; Amemiya S Nanoscale mechanism of molecular transport through the nuclear pore complex as studied by scanning electrochemical microscopy. J. Am. Chem. Soc 2013, 135, 2321–2329. [PubMed: 23320434]

(26). Nioradze N; Chen R; Kim J; Shen M; Santhosh P; Amemiya S Origins of nanoscale damage to glass-sealed platinum electrodes with submicrometer and nanometer size. Anal. Chem 2013, 85, 6198–6202. [PubMed: 23763642]

(27). Kim J; Kim B-K; Cho SK; Bard AJ Tunneling ultramicroelectrode: Nanoelectrodes and nanoparticle collisions. J. Am. Chem. Soc 2014, 136, 8173–8176. [PubMed: 24857267]

(28). Chen R; Balla RJ; Li ZT; Liu HT; Amemiya S Origin of asymmetry of paired nanogap voltammograms based on scanning electrochemical microscopy: Contamination not adsorption. Anal. Chem2016, 88, 8323–8331. [PubMed: 27426255]

(29). Fulian Q; Fisher AC; Denuault G Application of the boundary element method in electrochemistry: Scanning electrochemical microscopy. J. Phys. Chem. B 1999, 103, 4387–4392.

(30). Sklyar O; Wittstock G Numerical simulations of complex nonsymmetrical 3D systems for scanning electrochemical microscopy using the boundary element method. J. Phys. Chem. B 2002, 106, 7499–7508.

(31). Cornut R; Bhasin A; Lhenry S; Etienne M; Lefrou C Accurate and simplified consideration of the probe geometrical defaults in scanning electrochemical microscopy: Theoretical and experimental investigations. Anal. Chem 2011, 83, 9669–9675. [PubMed: 22081882]

(32). Gossage ZT; Simpson BH; Schorr NB; Rodriguez-L0pez J. Soft surfaces for fast characterization and positioning of scanning electrochemical microscopy nanoelectrode tips. Anal. Chem 2016, 88, 9897–9901. [PubMed: 27653997]

(33). Lefrou C A unified new analytical approximation for positive feedback currents with a microdisk SECM tip. J. Electroanal. Chem 2006, 592, 103–112.

(34). Liu B; Bard AJ Scanning electrochemical microscopy. 45. Study of the kinetics of oxygen reduction on platinum with potential programming of the tip. J. Phys. Chem. B 2002, 106, 12801–12806.

(35). Simeonov S; Schaffer TE High-speed scanning ion conductance microscopy for sub-second topography imaging of live cells. Nanoscale 2019, 11, 8579–8587. [PubMed: 30994121]

(36). Novak P; Shevchuk A; Ruenraroengsak P; Miragoli M; Thorley AJ; Klenerman D; Lab MJ; Tetley TD; Gorelik J; Korchev YE Imaging single nanoparticle interactions with human lung cells using fast ion conductance microscopy. Nano Lett. 2014, 14, 1202–1207. [PubMed: 24555574]

(37). Cornut R; Poirier S; Mauzeroll J Forced convection during feedback approach curve measurements in scanning electrochemical microscopy: Maximal displacement velocity with a microdisk. Anal. Chem 2012, 84, 3531–3537. [PubMed: 22385037]

(38). Shen M; Ishimatsu R; Kim J; Amemiya S Quantitative imaging of ion transport through single nanopores by high-resolution scanning electrochemical microscopy. J. Am. Chem. Soc 2012, 134, 9856–9859. [PubMed: 22655578]

(39). Chen R; Balla RJ; Lima A; Amemiya S Characterization of nanopipet-supported ITIES tips for scanning electrochemical microscopy of single solid-state nanopores. Anal. Chem 2017, 89, 9946–9952. [PubMed: 28819966]

(40). Wiebe N; Braun D; Lloyd S Quantum algorithm for data fitting. Phys. Rev. Lett 2012, 109, 050505. [PubMed: 23006156]

(41). Borgwarth K; Ebling DG; Heinze J Scanning electrochemical microscopy - a new scanning-mode based on convective effects. Ber. Bunsen-Ges. Phys. Chem 1994, 98, 1317–1321.

(42). Cornut R; Lefrou C New analytical approximation of feedback approach curves with a microdisk SECM tip and irreversible kinetic reaction at the substrate. J. Electroanal. Chem 2008, 621, 178–184.

(43). Huang BY; Li ZH; Li JY An artificial intelligence atomic force microscope enabled by machine learning. Nanoscale 2018, 10, 21320–21326. [PubMed: 30422134]

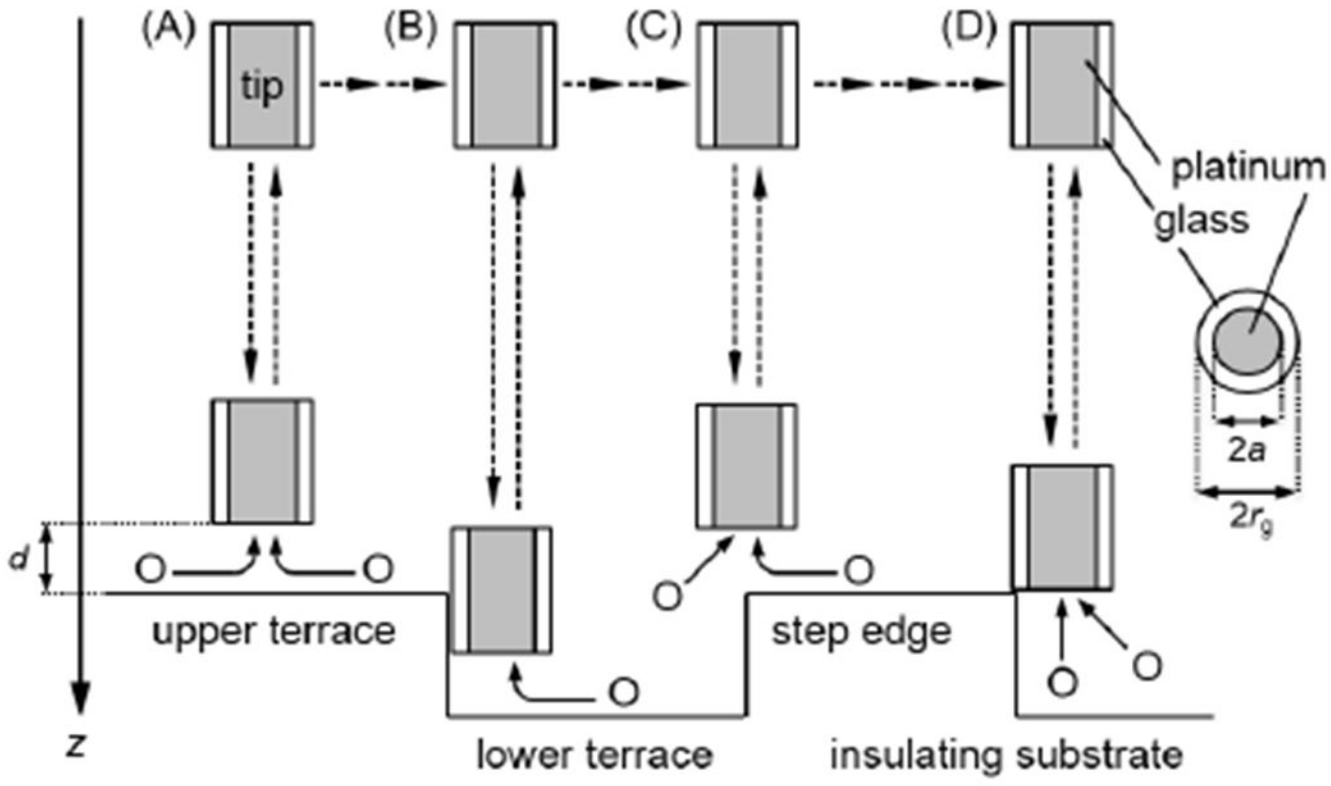

Figure 1.

Scheme of SECM imaging based on real-time analysis of approach curve at an insulating substrate with step edges under a diskshaped Pt tip with thin glass sheath. Dashed lines with arrows indicate the tip movement. Solid lines with arrows indicate diffusion of redox species, O, to the tip.

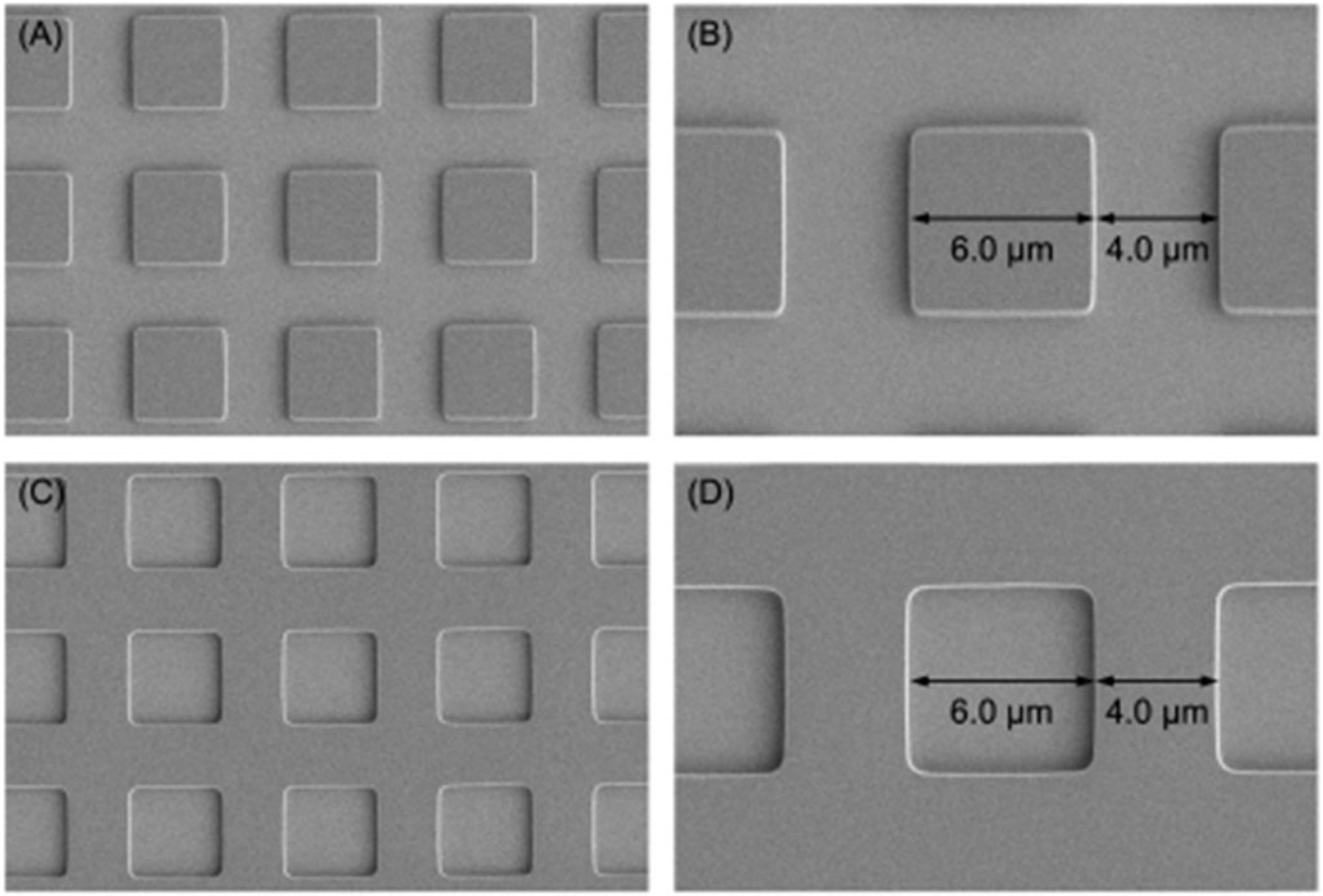

Figure 2.
SEM images of (A) and (B) protrusions and (C) and (D) recessions of insulating substrate.

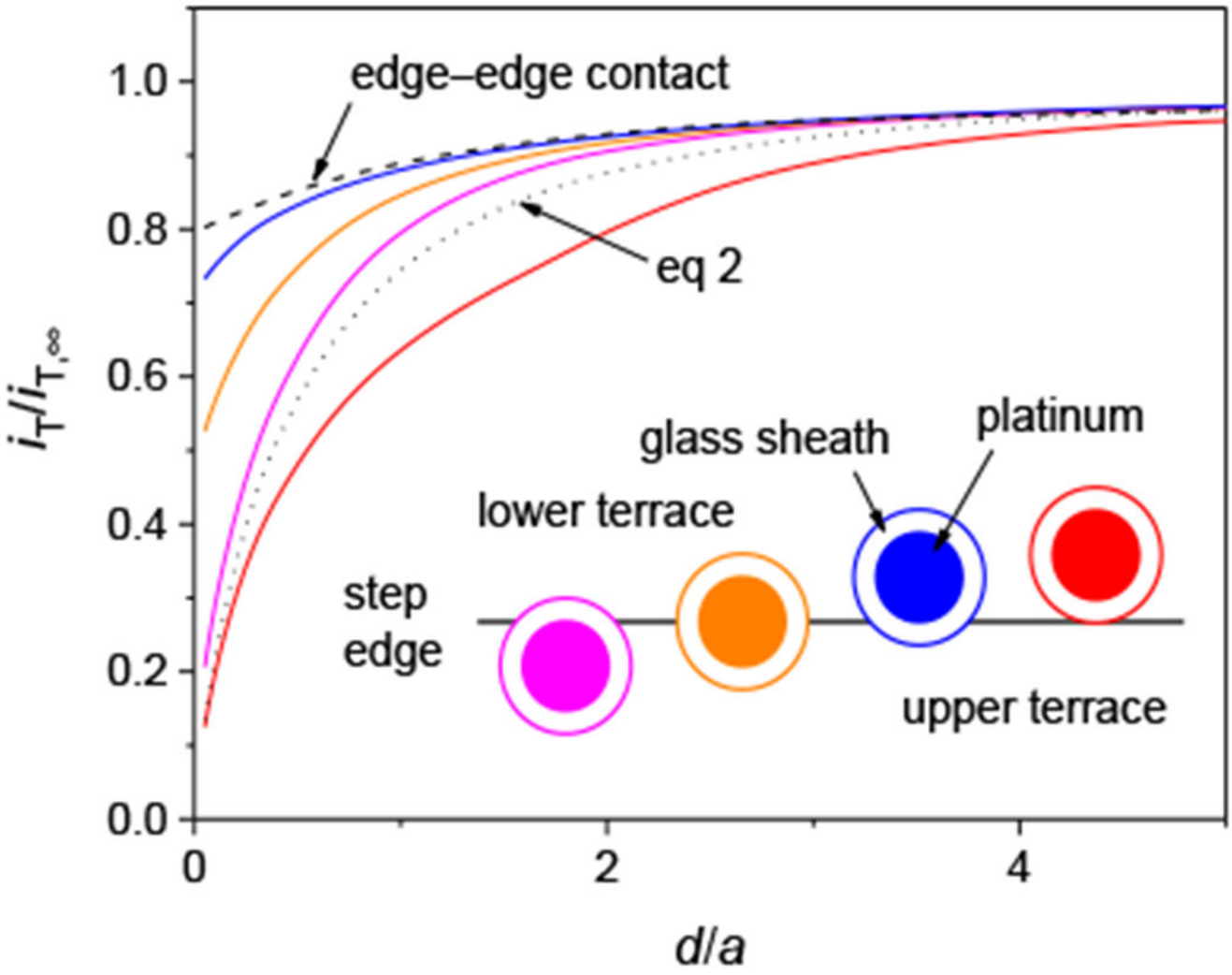

Figure 3.

Characteristic approach curves (solid lines) simulated at various lateral tip positions over a step edge as depicted in the inset (top view) by using the same colors. The most negative approach curve (red line) was shifted laterally by the depth of step edge (2*a*) to obtain the approach curve of edge–edge contact (dashed line).

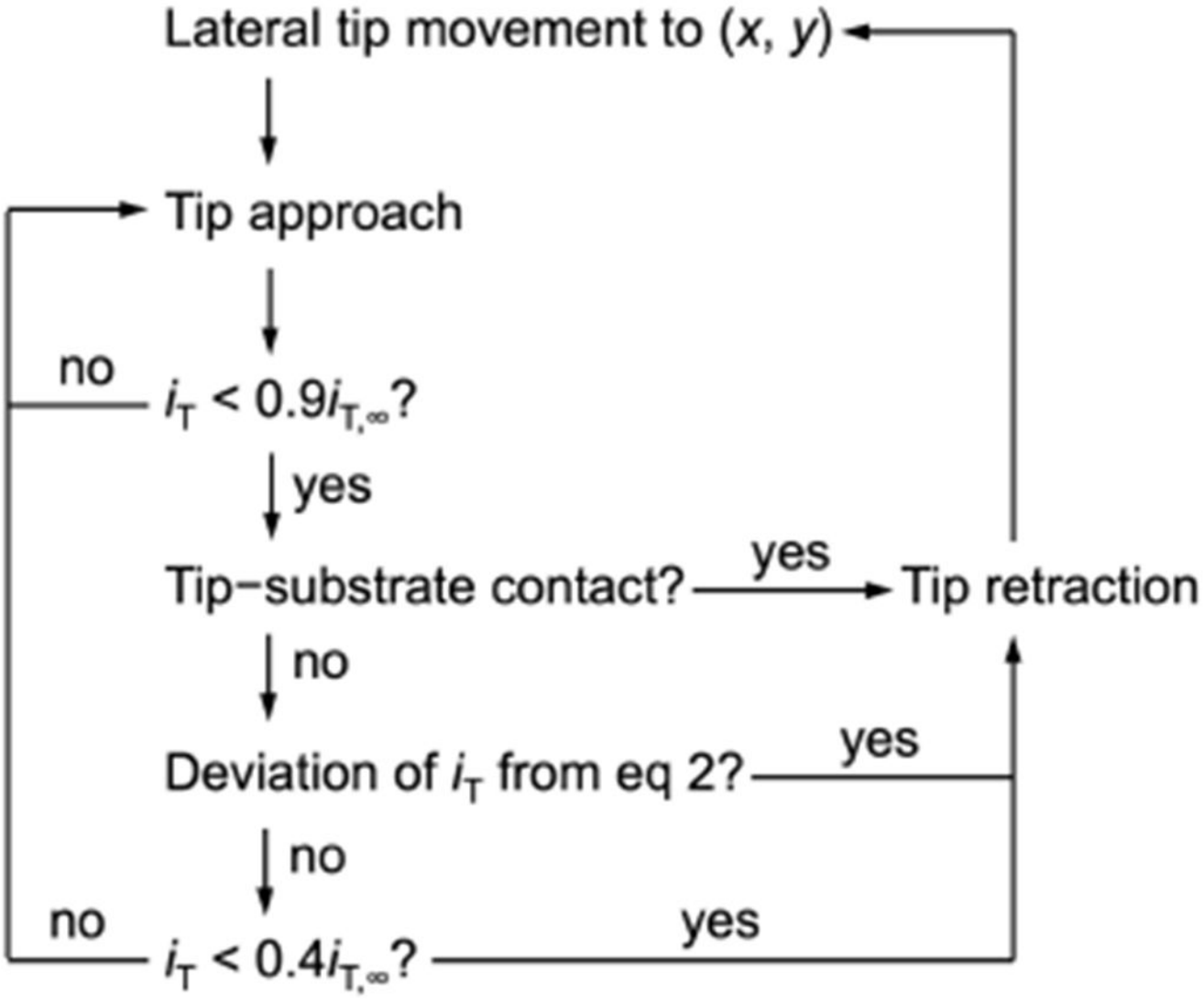

Figure 4.
Flow chart of real-time analysis of approach curve.

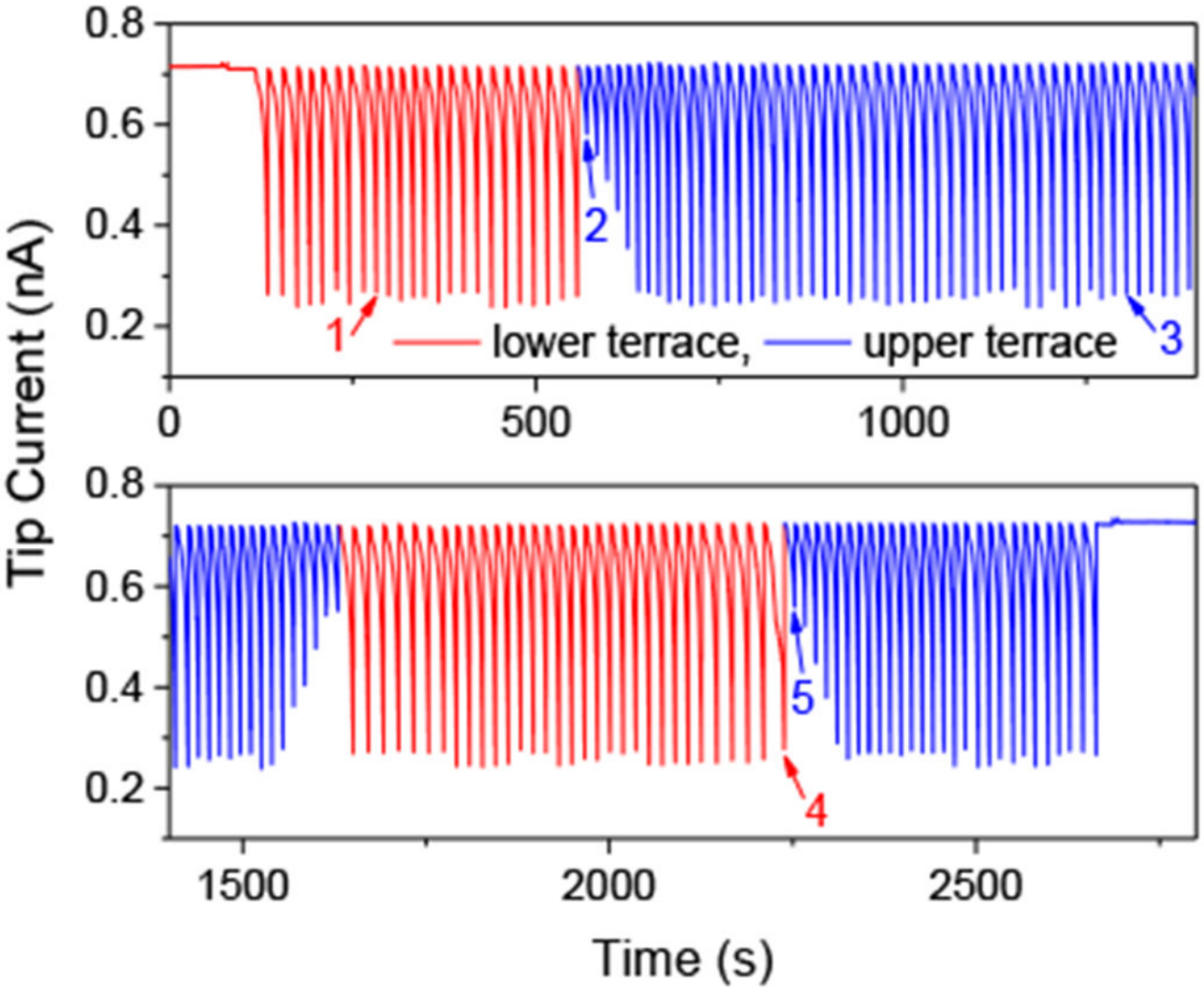

Figure 5.

The tip current during line scan based on tip approach to lower (red lines) or upper (blue lines) terraces of the substrate with step edges in 10 mM $Ru(NH_3)_6^{3+}$ and 1 M KCl. Arrows indicate characteristic approach curves shown in Figure 7.

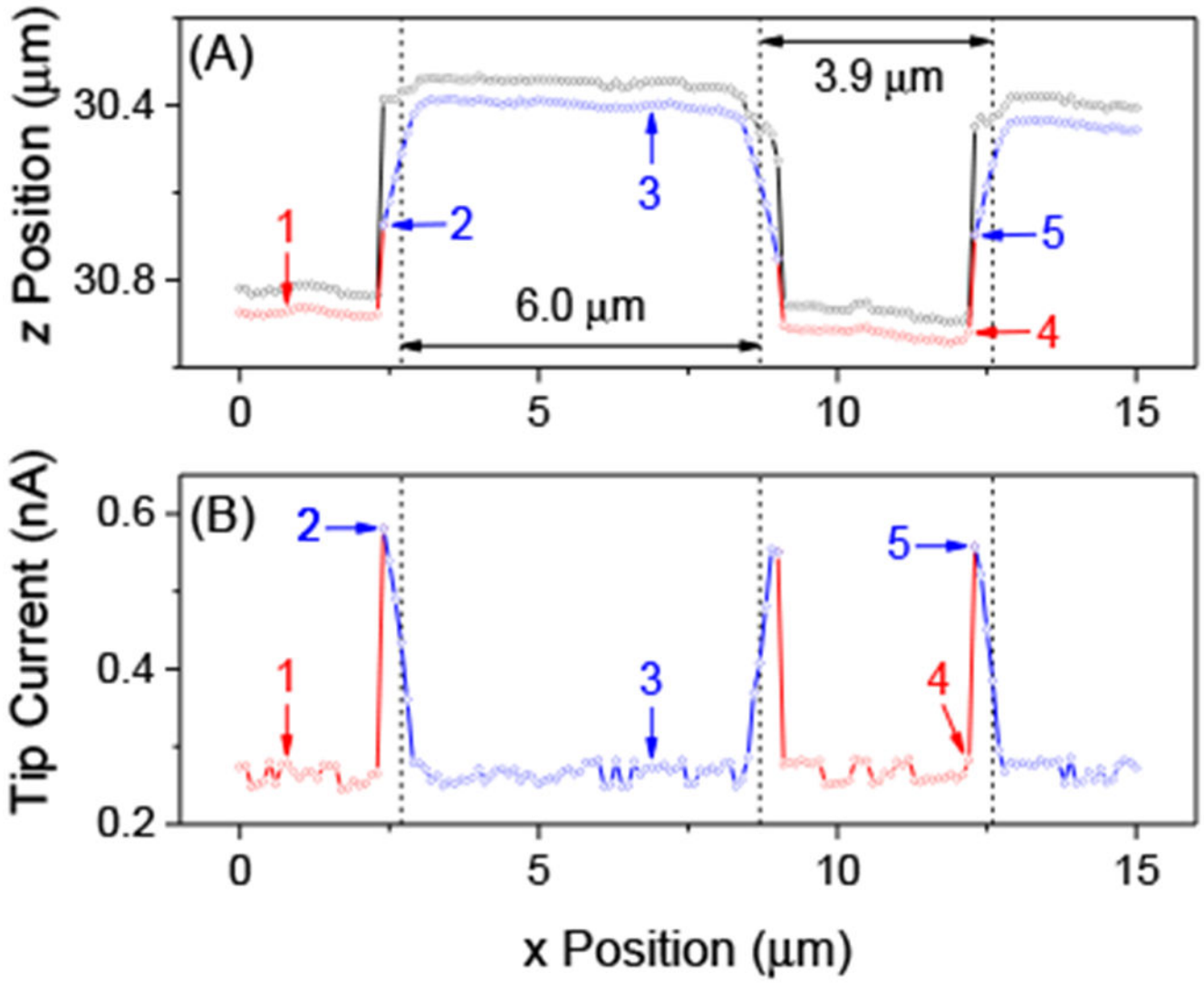

Figure 6.

(A) The *z* positions of substrate determined by fitting approach curves with eq 2 (red and blue circles) and the final *z* positions of approach curves (black circles) with the corresponding tip current in part (B).

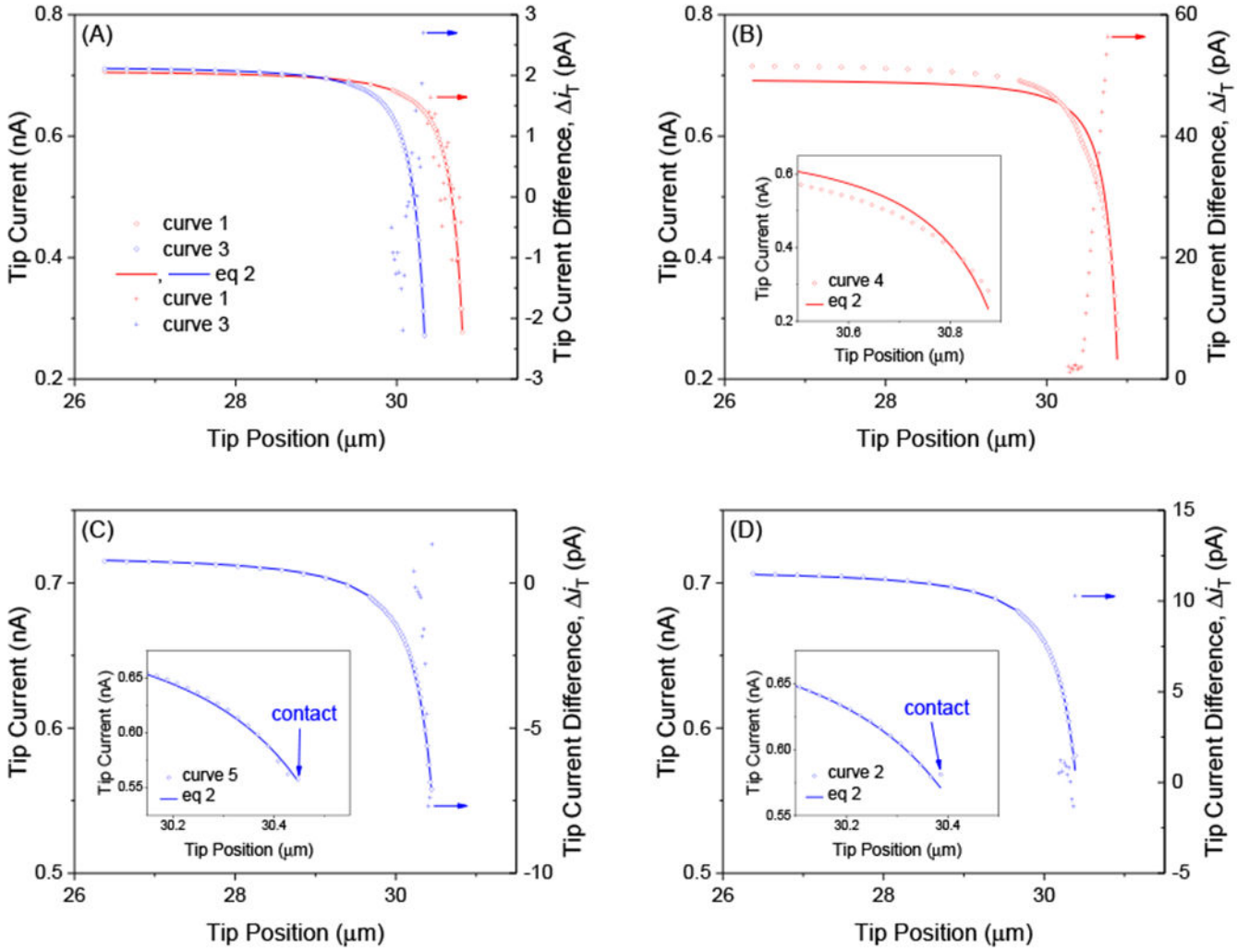

Figure 7.

Experimental approach curves (circles) at (A) upper and lower terraces far from the step edge without contact, (B) lower terrace adjacent to the step edge without contact, (C) step edge in avoidable contact with the edge of tip, and (D) step edge in unavoidable contact with the edge of tip in 10 mM $Ru(NH_3)_6^{3+}$ and 1 M KCl. Each curve is indicated by an arrow in Figure 5. Theoretical curves (lines) were obtained by the best fit of eq 2. Crosses are Δi_T values defined by eq 3. Insets show the last part of the experimental and theoretical approach curves.

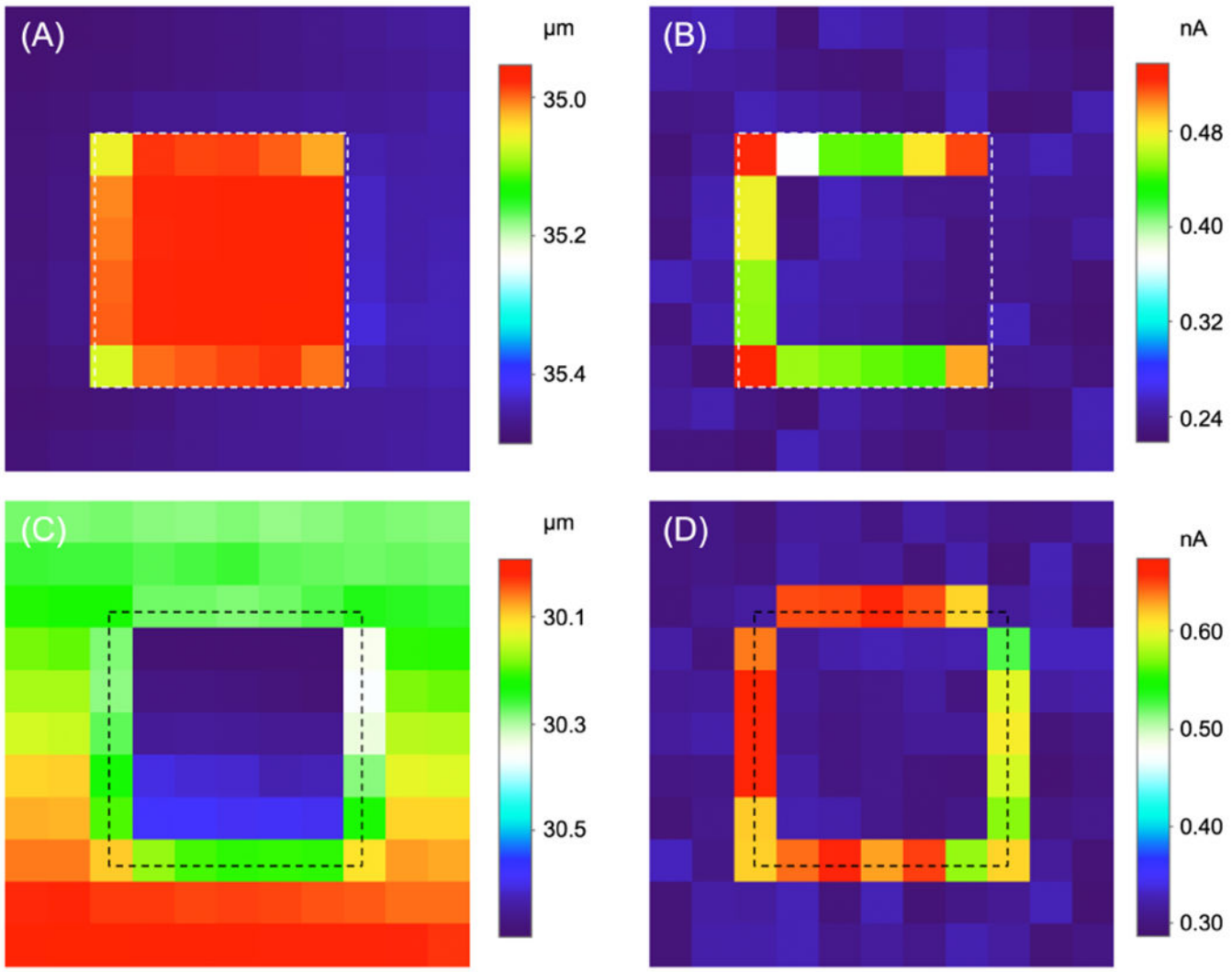

Figure 8.

11 μm × 11 μm images based on (A) topography and (B) current at a protrusion and (C) topography and (D) current at a recession on insulating substrates in 10 mM $Ru(NH_3)_6^{3+}$ and 1 M KCl. Each pixel is equivalent to 1 μm × 1 μm. The position of step edges is represented by 6 μm × 6 μm dashed boxes. The tip was scanned laterally from the left bottom corner and stepped upward after each line scan.

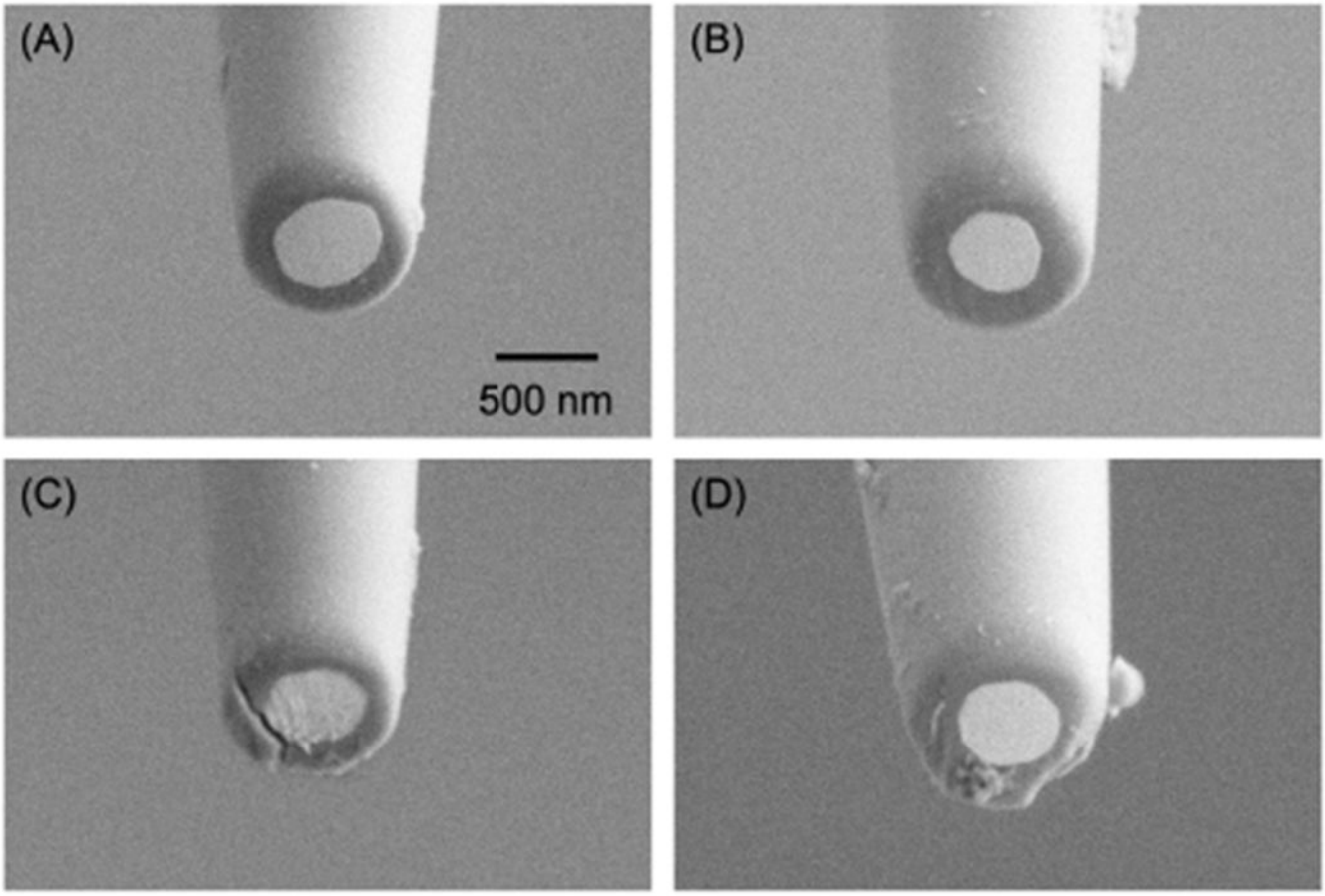

Figure 9.
SEM images of (A) and (B) undamaged and (C) and (D) damaged Pt nanotips after SECM imaging with low and high threshold values of −0.1 and −0.5 pA/nm for Aslope, respectively. Figure S-1 shows SEM images of these tips just after FIB milling.